Numerical modeling of limiting oxygen index apparatus for film type fuels

Amit Kumar*,† and James S. T'ien#

†Indian Institute of Technology Madras, Chennai, Tamilnadu, India

#Case Western Reserve University, Cleveland, Ohio, USA

Submission June 13, 2012; Revised Submission September 6, 2012; Acceptance September 11, 2012

ABSTRACT

A detailed three-dimensional numerical model is used to compute the flow pattern and the flame behavior of thin solid fuels in a rectangular column that resembles a standard Limiting Oxygen Index (LOI) device. The model includes full Navier-Stokes equations for mixed buoyant-forced flow and finite rate combustion and pyrolysis reactions so that the sample LOI can be computed to study the effect of feeding flow rate, sample width and gravity levels. In addition to the above parameters, the sample location in the column and the column cross-sectional area are also investigated on their effect on the ambient air entrainment from the top.

Keywords: Limiting Oxygen Index, LOI Apparatus, test method ASTM D2863, Air Entrainment, Numerical Modeling, CFD, Thin Fuel, Flame spread, Gravity Effect

1. INTRODUCTION

Limiting Oxygen Index (LOI) is a commonly used measure of material flammability. It is defined in ASTM D2863 [1] as "the minimum level of oxygen, expressed as volume percent, in a flowing mixture of oxygen and nitrogen that will just support candle like flaming combustion of a material initially at room temperature under specific conditions of test method". The schematic of the apparatus used for testing film type fuel is shown in fig. 1(A). The conventional apparatus comprises of a glass test column (75 mm diameter and 450 mm high) which is open to the atmosphere at the top. A gas control and metering system supplies the oxygen/nitrogen mixture from the bottom and a specimen holder to keep specimen vertical. The testing procedure consists of passing through the column, oxygen and nitrogen mixture of varying the composition at a controlled rate to determine whether material burns or extinguishes at each

*Corresponding author: Amit Kumar, National Center for Combustion Research and Development, Department of Aerospace Engineering, Indian Institute of Technology Madras, Chennai-600036-Tamilnadu INDIA, TEL: (+91)-44-22574019, FAX: (+91)-44-22574002, email: amitk@ae.iitm.ac.in

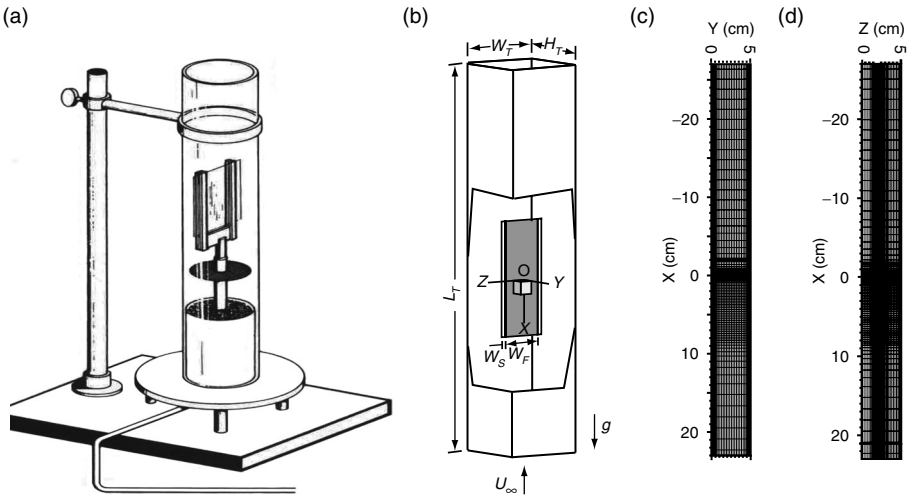

Figure 1: (A) The schematic of the LOI device for film type fuels. (B) Schematic of three-dimensional column with rectangular cross-section used to simulate the flow and combustion phenomenon in a Limiting Oxygen Index device. (C) & (D) computational grid structure in *XY* and *XZ* planes.

concentration. The typical prescribed gas velocity of 30 mm/s–50 mm/s at the base of column at standard temperature of 273 K and pressure 101.3 kPa is prescribed.

At the time of development of the test, preliminary studies by Fenimore and Martin [2] showed that Limiting Oxygen Index would be fairly constant within the velocity range 3–12 cm/s, a conclusion which was later questioned by several investigators [3–5]. Wharton [4] reports several prior investigations on the subject. Some found LOI value to increase non-linearly with increase in gas flow velocity, while others reported little or no dependence of LOI on gas flow velocity. In his own work Wharton [4, 5] tried to resolve the above-observed discrepancy. He observed that ambient air could enter the column under certain condition and that the extent of entrainment depended on gas velocity. Wharton [4] argued based on his experimental observations that for the materials with LOI less than that of ambient air, the gas mixture could be augmented by entrained denser ambient air from the open top exit of the column that results in a much lower LOI value where as in cases where LOI is more than that of ambient air, the latter being denser than air cannot be displaced easily. McIllhager and Hill [6] conducted a study on polypropylene films where the gas flow rate was varied from 10.6 l/min (4 cm/s) to 20 l/min (~7.55 cm/s). To their surprise LOI showed an upward trend with increase in volumetric flow rate of the gas. The LOI increased first from 19.8% to 21.5% over the flow rate range 10.6 l/min to 15 l/min and then remained at about 21.5% oxygen over flow rate range of 15 l/min–20 l/min. Although the authors themselves did not make any measurements on the degree of entrainment, they did acknowledge the observations of Wharton [5] but did not consider entrainment to be sufficient to influence the trend they observed. In the work by Zhevlakov *et al* [7] on

PMMA and fiber glass specimens of cross-section 0.2 cm × 0.3 cm and length 15–20 cm, LOI for which the flame stopped propagating along the side surface, increased with increase in forced flow velocity over the range 0–6 m/s. Thus in the various investigations there is no consensus on the dependence of LOI on flow velocity.

So far the study of flow influence on the LOI device has been limited to global experimental measurements. There has not been any detailed experimental nor numerical study on this device. Here in this work an up-to-date three dimensional model of opposed flow flame spread is used to investigate the downward burning and extinction phenomenon in an LOI device for thin-film type fuels. The focus of this work is to study the flow field inside an LOI column, in particular the extent of the ambient air entrainment, the flame extinction mechanism and the oxygen limit for thin- fuels. Specifically, the following parameters are varied: inlet flow velocity and fuel sample width. We note that although LOI device normally operates in normal earth gravity, reduced gravity can have implication for space application. Therefore, flow field associated with microgravity ($0g_e$) opposed flow spreading flame, flame spread rates and extinction limits are also studied for the above mentioned parameters.

2. GEOMETRY AND CONFIGURATION

Most LOI devices use a cylindrical column as shown in Figure 1(A). In this study, however, a three-dimensional column with rectangular cross-section is used as shown in Fig. 1(B). The rectangular column simplifies the specification of the boundary conditions since rectangular numerical grids used are more convenient for flat fuel samples. It is believed that the spreading flame characteristics, the flame spread rates, the flow field and the flame extinction which depend primarily on interaction between flow and the fuel surface will be similar between the two types of columns. Fig. 1(B) shows the configuration and the dimensions of the base case. A column of length ($\bar{L}_T$) 50 cm having uniform internal cross-sectional dimension of 10 cm × 10 cm is used. In this three-dimensional geometry, X coordinate is along the axis of the column, Y coordinate is perpendicular to the sample surface and Z coordinate is parallel to the sample surface. There is a symmetry plane at half column height ($Y = 0$), which is also plane of solid fuel surface. Unless specified, the fuel sample is located approximately half way between the entrance and the exit of the column. The fuel specimen is 0.0165 cm thick (area density 4.62×10^{-3} g/cm^2) and 15 cm long ($\bar{L}_F$), and is bounded by inert strips on each sides with strip width ($\bar{W}_S$) 0.6 cm along the length. The origin (O) of the co-ordinate system is located at the center ($Y = 0$, $Z = 0$) of the rectangular cross-section, $X = 0$ is located at 95% of fresh fuel thickness (assumed to be the solid fuel pyrolysis front) along the tunnel axis (X-axis). Another symmetry plane is the $Z = 0$ plane, oriented perpendicular to fuel surface at half tunnel width. The width ($\bar{W}_F$) of fuel sample can vary from 0.5 cm to 5 cm. Symmetry consideration about planes $Z = 0$ and $Y = 0$ reduces the computational domain to one quarter the size of full three-dimensional flow field. The domain along Y, extends from $Y = y_{\min} = 0$, at the fuel surface to $Y = y_{\max} = \bar{H}_T/2$ at column wall and along Z, the domain extent is from $Z = z_{min} = 0$ at fuel half width to $Z = z_{\max} = \bar{W}_T/2$ at column wall. Oxygen and nitrogen gas mixture of desired composition enters from the column base with uniform velocity $\bar{U}_\infty$. In the flame fixed coordinates the flame is stabilized on the fuel surface near the pyrolysis front. At $Z = 0$

flame is anchored close to $X = 0$ located 27 cm below the column exit $X = x_{min}$ ($\bar{x}_{min} = -27$ cm). $X < 0$ is downstream of the flame and $X > 0$ is upstream of flame. It is assumed that 7 cm of the fuel specimen is upstream of the flame over which the velocity profile develops as flow approaches the flame. In this co-ordinate system, the fuel approaches flame with a velocity V_f and the flow enter the column (at $X = x_{min}$ ($\bar{x}_{min} = 23$ cm)) with a relative velocity of $\bar{U}_\infty - V_f$, where $\bar{U}_\infty$ is the prescribed inlet velocity at the bottom of the column. The gravity vector is directed downwards along $X > 0$.

3. NUMERICAL MODEL AND NUMERICAL SCHEME

The numerical model consists of steady state governing equations in gas and solid phases formulated for the opposed-flow spread in flame-fixed coordinate system. In reality as flame spreads, the finite length of fresh fuel ahead of flame decreases slowly in time. But the time scale of this change of the entrance length is much longer than the response time of the flame. A quasi-steady approximation is made here. In the present formulation a steady spread is considered for a fixed fuel length ahead of the flame. The computed result is assumed to represent the instantaneous flame at that location. The formulation of governing equations is carried out in three-dimensions for realistic simulation of the LOI apparatus.

3.1. Gas phase model

The gas-phase consists of three-dimensional governing equations of full Navier-Stokes equations for laminar flow along with the conservation equations of mass, energy and species. The specie equations are for fuel vapor, oxygen, carbon dioxide and water vapor. A one-step, second-order finite rate Arrhenius reaction between fuel vapor and oxygen is assumed. The governing equations are presented in non-dimensional form. In these equations, V_f, X_e, the reference properties (with * superscript) and the variables with overhead bar indicate dimensional quantities. The rest are non-dimensional quantities. The length scale chosen for normalization is the thermal length, $L_R = \alpha^*/\bar{U}_R$ (here α^* is the reference gas thermal diffusivity) which is obtained by considering the balance of convection and conduction in the gas-phase flame stabilization zone. The reference velocity, $\bar{U}_R$ (defined later) is used to normalize velocity and ambient temperature, $\bar{T}_\infty$ is used to normalize temperature. Pressure is referenced to the ambient value of 1atm ($\bar{P}_\infty$) and is normalized as $P = (\bar{P} - \bar{P}_\infty)/(\rho^* \bar{U}_R^2)$. All thermal and transport properties are normalized by their values at the reference temperature, T^* (1250 K), which is the mean of the adiabatic flame temperature in air and ambient temperature. Specific heats are a function of temperature for each species and obtained from standard references. The gas phase is assumed to follow ideal gas law,

$$\rho = \frac{\bar{P}}{\rho^* \bar{R}_u \bar{T} \sum_i (Y_i / M_i)}, \quad i = F, O_2, CO_2, H_2O, N_2.$$

.

The transport properties are modeled following Smooke and Giovangigli [8].

$$\mu = T^{0.7}, \quad \kappa / c_p = T^{0.7}, \quad \rho D_i = T^{0.7}, \quad i = F, O_2, CO_2, H_2O, N_2$$

The non-dimensional governing equations and the boundary conditions in the gas phase are summarized below.

Continuity equation

$$\nabla \cdot \left(\rho \vec{U} \right) = 0$$

X-Momentum Equation

$$\nabla \cdot \left[\rho u \vec{U} - \left(\frac{\mu}{\mathrm{Re}} \right) \nabla u \right] = -p_x + \left(\frac{1}{\mathrm{Re}} \right) \left\{ \left[\frac{1}{3} \mu u_x - \frac{2}{3} \mu \left(v_y + w_z \right) \right]_x + \left[\mu v_x \right]_y + \left[\mu w_x \right]_z \right\} + \left(\frac{U_B}{U_R} \right)^3 \frac{\left(\rho - \rho_\infty \right)}{\left(\rho_f - \rho_\infty \right)} g$$

Y-Momentum Equation

$$\nabla \cdot \left[\rho v \vec{U} - \left(\frac{\mu}{\mathrm{Re}} \right) \nabla v \right] = -p_y + \left(\frac{1}{\mathrm{Re}} \right) \left\{ \left[\mu u_y \right]_x + \left[\frac{1}{3} \mu v_y - \frac{2}{3} \mu \left(u_x + w_z \right) \right]_y + \left[\mu w_y \right]_z \right\}$$

Z-Momentum Equation

$$\nabla \cdot \left[\rho w \vec{U} - \left(\frac{\mu}{\mathrm{Re}} \right) \nabla w \right] = -p_z + \left(\frac{1}{\mathrm{Re}} \right) \left\{ \left[\mu u_z \right]_x + \left[\mu v_z \right]_y + \left[\frac{1}{3} \mu w_z - \frac{2}{3} \mu \left(u_x + v_y \right) \right]_z \right\}$$

where

$$\mathrm{Re} = \frac{\bar{L}_R \bar{U}_R \rho^*}{\mu^*}, \quad L_R = \frac{\alpha^*}{\bar{U}_R}$$

$$\bar{U}_R = \left| \bar{U}_\infty + \bar{U}_B - V_f \right|$$

$\bar{U}_B = \left[g_R \beta_R \left(T_\infty - T_F \right) \alpha^* \right]^{1/3}$ is the reference buoyancy induced velocity and $\bar{U}_\infty$ is the imposed forced velocity at the inlet of the column. Both $\bar{U}_B$ and $\bar{U}_\infty$ are taken negative as the inflow and induced buoyant flow is in the negative x direction and V_f positive.

Specie equation

$$\nabla \cdot \left[\rho Y_i \vec{U} - \left(\frac{1}{Le_i} \right) \left(\rho D_i \nabla Y_i \right) \right] = \dot{\omega}_i''' \qquad i = F, O_2, CO_2, H_2O, N_2$$

where, Lewis number for species

$$Le_{Fi} = 1.0 \quad Le_{O2} = 1.11 \quad Le_{CO2} = 1.39 \quad Le_{H2O} = 0.83 \quad Le_{N2} = 1.0$$

$$\text{and } \dot{\omega}_i''' = f_i \dot{\omega}_F''' = f_i \; Da \rho^2 Y_F Y_{O2} \exp\left(\frac{-E_g}{T}\right) \text{ and } Da = \frac{\bar{B}_g \rho^* \alpha^*}{\bar{U}_R^2}$$

f_i = stoichiometric mass ratio of species i and fuel

$E_g = \bar{E}_g / \bar{R}_u \bar{T}_\infty$ non-dimensional gas-phase activation energy (45.3)

(Note the number in the parenthesis is the numerical value of the quantity defined).

$\bar{B}_g$ = gas-phase pre-exponential factor (1.58×10^9 m^3/kg/s)

The solid fuel is cellulose with chemical formula $C_6H_{10}O_5$. The stoichiometric combustion of fuel in air can thus be written as:

$C_6H_{10}O_5 + 6\ (O_2 + 3.76\ N_2) \rightarrow 6\ CO_2 + 5\ H_2O + 22.56\ N_2$

For the above one-step cellulose and air stoichiometric reaction, the stoichiometric ratios are: $f_F = -1, f_{O2} = -1.1852, f_{CO2} = 1.6296, f_{H2O} = 0.5556, f_{N2} = 0$

Energy Equation

$$c_p \nabla \cdot \left[\rho T \vec{U} - \left(\frac{\kappa}{c_p} \nabla T\right)\right] = \sum_{i=1}^{N} \left(\frac{1}{Le_i}\right) \rho D_i c_{p,i} \left(\nabla Y_i \cdot \nabla T\right) - \sum_{i=1}^{N} \dot{\omega}_i''' h_i + \nabla c_p \cdot \nabla T \left(\frac{\kappa}{c_p}\right)$$

where $$c_p = \sum_{i=1}^{N} c_{p,i} Y_i \;, \; h_i = \frac{(\bar{h}_i^0 + \int_{\bar{T}_0 = 298\,K}^{\bar{T}} \bar{c}_{p,i} d\bar{T})}{(c_p^* \bar{T}_\infty)}$$

The boundary conditions in the gas phase are presented below.

At $X = x_{\max}$ (*upstream or inlet*)

$$u = (\bar{U}_\infty - V_f) / \bar{U}_R \,, v = 0, w = 0, T = 1$$

$$Yo_2 = Yo_{2,inlet}, Y_i = 0 \ (i = F, CO_2, H_2O)$$

At $X = x_{\max}$ (*downstream or exit*)

$$u_x = 0, v_x = 0, w_x = 0$$

if $u > 0 \quad T = 1, \quad Y_{O2} = Y_{O2,\infty}, \quad Y_i = 0$ (*combstion products assumed negligible*)

if $u \le 0 \quad T_x = 0, \ (Y_i)_x = 0 \quad$ *where* $i = O_2, CO_2, H_2O, F$

At $Y = 0$ (*Fuel surface or Y symmetry plane*)

$$u = -V_f / \bar{U}_R \,, v = v_w \,, w = 0 \,, \; T = T_s$$

$$\dot{m} Y_{F,w} = \dot{m} + \frac{\rho D_F}{Le_F} \left(\frac{\partial Y_F}{\partial y}\right)_w \,, \quad \dot{m} Y_{i,w} = \frac{\rho D_i}{Le_i} \left(\frac{\partial Y_i}{\partial y}\right)_w \quad (i = O_2, CO_2, H_2O)$$

Here the fuel vapor mass flux $\dot{m}$, blowing velocity v_w, and surface temperature T_s as functions of x and z are determined by the coupled solutions with the solid phase equations

For regions of complete fuel burnout (no inert)

$$u_y = 0\ ,\ v = 0,\ w_y = 0,\ T_y = 0,\ \left(Y_i\right)_y = 0$$

At $Y = y_{\max}$ *at turnel wall*

$$u = -V_f / \bar{U}_R,\ v = 0,\ w = 0$$

$$T = 1,\ \left(Y_i\right)_y = 0 \quad (i = F, O_2, CO_2, H_2O)$$

At $Z = z_{\min}$ (*Z symmetry plane*)

$$u_z = 0,\ v_z = 0,\ w = 0$$

$$T_z = 0,\ (Y_i)_z = 0 \quad (i = F, O_2, CO_2, H_2O)$$

At $Z = z_{\max}$ *i.e. at tunnel wall*

$$u = -\ V_f / \bar{U}_R,\ v = 0,\ w = 0$$

$$T = 1,\ \left(Y_i\right)_z = 0 \quad (i = F, O_2, CO_2, H_2O)$$

3.2. Solid phase model

The solid is assumed to be thin (both thermally and aerodynamically). For a thermally thin fuel the temperature is constant across its thickness. Another implication of thermally thin assumption is that conduction along the length and across the width of solid can be neglected. The aerodynamically thin condition implies that the flame standoff distance is much greater than the thickness of the solid so that the solid phase boundary conditions are applied at the surface *i.e.* $Y = 0$.

The thin solid fuel model comprises of equations of continuity and energy in two-dimensions along with a solid fuel pyrolysis law. The solid considered here is a cellulosic material with half thickness $\bar{\tau} = 0.0825$ mm, 50% of which is inert (a practical example is fiber reinforced fuel). The solid is assumed to burn ideally *i.e.* it vaporizes to form fuel vapors without melting. The pyrolysis of fuel is modeled using a one-step, zeroth-order Arrhenius kinetics and radiation loss from the solid included. The pyrolysis model relating fuel vapor mass flux from the solid to surface temperature can be represented in non-dimensional form as

$$\dot{m} = A_s \rho_s \exp\left(\frac{-E_s}{T_s}\right) = \rho v_w$$

where, $E_s = \bar{E}_s / \bar{R}_u \bar{T}_\infty$ = non-dimensional solid-phase activation energy (50.3)

$\bar{A}_s = A_s \bar{U}_R$ = gas-phase pre-exponential factor (3.8×10^7 cm/s)

The solid density ($\overline{\rho}_s$ = 0.506 g/cm^3) is taken as a constant while thickness of the fuel (h) is assumed to change with pyrolysis. The blowing velocity distribution (v_w) along the fuel surface is determined from the fuel vapor mass flux and the gas phase density at the surface.

In the flame fixed coordinates, the fuel feeds into the domain at a speed V_f. Where, V_f is the flame-spread rate and is an eigen value of this problem. The governing equations for the fuel for steady spread are as follows.

Mass conservation:

$$\dot{m} = \rho_s V_f \left(h\right)_x$$

Combining the pyrolysis relation with mass conservation, the relation between fuel thickness and surface temperature is obtained as

$$\left(h\right)_x = \frac{A_s}{V_f} \exp(\frac{-E_s}{T_s})$$

Energy equation:

$$q_c + \frac{q_r^y}{Bo} + \Gamma\left(hT_s\right)_x = \Gamma\left(h\right)_x \left[\left(1-c\right)T_L + \left(-L\right) + cT_S\right]$$

where $$\Gamma = \frac{\overline{\rho}_s \overline{c}_s V_f}{\rho^* c_P^* \overline{U}_R}, \quad c = \frac{\overline{c}_p}{\overline{c}_s} \text{ and } \quad Bo = \rho^* c_p^* U_R / (\sigma T_\infty^3)$$

On the left-hand side of the energy equation, the first term is the conductive heat flux from the gas phase (q_c). In the solid phase energy equation the terms describing conduction through the solid fuel have been neglected based on thermally thin assumption discussed earlier. The second term is the radiation term due to solid phase radiation loss and $q_r^y = -\varepsilon(T_s^4 - 1)$. The third term of the left-hand side represents bulk heat up term and the right-hand side represents the energy change due to the latent heat of vaporization of the fuel. The fuel has latent heat, $\overline{L}$ = 180 cal/g, specified at $\overline{T}$ = 300 K and constant specific heat, $\overline{c}_p$ = 0.33 cal/g/K. Flame (gas) radiation is neglected in this work. This will be discussed further later.

The boundary conditions for the solid phase governing equations are the prescribed fuel thickness and the surface temperature at fuel leading edge upstream of flame at ($x = x_0$)

i.e at $x = x_0$ (*leading edge of fuel sample upstrem of flame*)

$$T_s = 1, \quad h = \overline{\tau} / \overline{L}_R$$

The above set of governing equations and boundary conditions complete the mathematical formulation and is ready to be solved numerically.

The system of coupled elliptic partial differential equations for the flow and combustion in the gas phase is solved numerically by an in-house code using SIMPLER algorithm [9]. The nonlinear equation sets are discretized using a finite-volume based difference technique. The velocities are stored at staggered grid locations with respect to scalar variables. The resulting set of algebraic equations is solved by sweeping plane-by-plane in each direction. Along each plane, the line-by-line procedure is used, which is a combination of Gauss-Seidel and the tri-diagonal matrix algorithm (TDMA). In addition, the gas-phase system is coupled to the sold-phase equations, which are solved by finite-difference technique. The steady flame spread rate (the eigenvalue of the whole system) is determined iteratively using bisection method to force and the pyrolysis front (95% of the fresh fuel thickness) to occur at $X = 0$, $Z = 0$.

The grid structure for this one-quarter domain is shown in fig.1 (C, D). Fig. 1(C) shows mesh on *XY* plane. The grid node distribution is non-uniform to account for presence of tunnel walls and two-dimensional fuel sample. Along *Y* direction the grid nodes are clustered at the fuel surface ($Y = 0$) to capture the flame structure and transport processes with adequate accuracy. The smallest grid size at this location is 0.05 thermal lengths, small enough to resolve the flame stabilization zone structure hence capable to address the flame extinction limit in question here. The grid expands away from fuel surface up to some intermediate distance and then contract to give clustered grid structure at the tunnel wall that are needed to resolve the gradient in velocity field. The grid node distribution along *X* is more complex due to the presence of finite size fuel specimen. The grid nodes are clustered around $X = 0$, which is near the pyrolysis front and also the flame-anchoring region. Here also the minimum grid size is 0.05 thermal lengths to accurately resolve the flame structure in the region. The grids expand away from $X = 0$ both in upstream and downstream directions. Fine grid structure in the burnout region is used to resolve the burnout location. Although it is difficult to ensure equally fine cells across the fuel width at the all pyrolysis front and burnout locations, in general grids are fine enough in the region. Grid nodes also cluster at the leading and the trailing edge of the fuel sample. Figure 1(D) shows *XZ* mesh. In *Z* direction fine grids are used near the column wall, metal strip gas interface and fuel and metal strip interface to ensure adequate local resolution. Grid independence check has been performed [9]. Before addressing the LOI device, theprediction capability of the model was assessed by simulating the experiments of Olson [10]. Olson carried out experiments on opposed flow flame spread over thin cellulosic fuel strips of half thickness 3.8×10^{-3} cm and width 3 cm in both normal gravity ($1g_e$) and 5s drop tower microgravity ($0g_e$) environments.The simulations were carried out using appropriate fuel properties and kinetic parameters. Figure 2 shows a comparison of numerical predictions with the experimental values. The computed flame spread rates predict the experimental trend both qualitatively and quantitatively. The deviation of numerical prediction from experimental values is larger at higher oxygen levels. This is due to the use of single

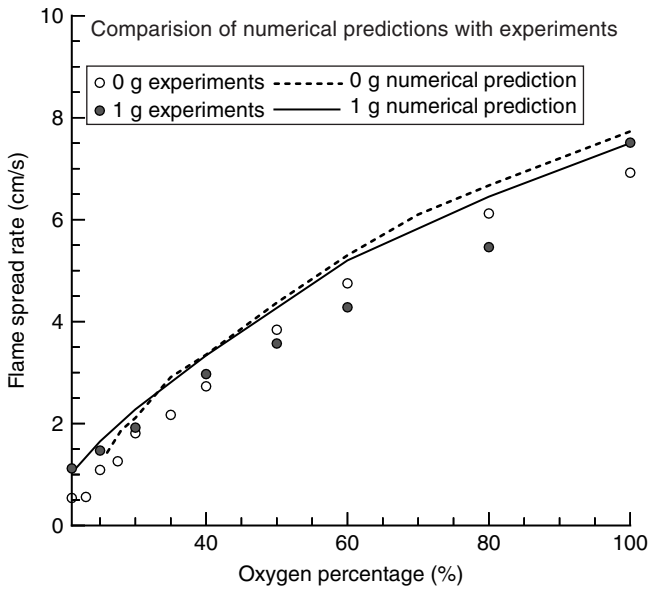

Figure 2: A comparison of prediction of flame spread rate from the 3D numerical model with the experiments of Olson [10] over a wide range of Oxygen percentage (21 to 100).

step chemistry in the present model which is expected to over predict flame temperatures at higher oxygen levels. However, at low oxygen levels, the agreement between numerical predictions and experiments can be considered reasonably good.

In simulation of the LOI apparatus, since the column size, fuel dimensions and position are specified dimensionally and the governing equations solved on non-dimensional mesh, the number of grid nodes varies from case to case. For a typical case of simulating normal gravity flame under forced opposed flow of 5 cm/s at 25% oxygen a mesh size of 140 × 44 × 40 (246,400 nodes) was used. The computational time for 1000 iterations on Compaq DS20E workstation at single user load is about 7 hours. Typically 4000–5000 (or more) iterations may be required to achieve convergence.

4. RESULTS

4.1. Flame and flow patterns in a LOI device: the base case

Figure 3 shows the simulated burning of fuel specimen inside the column under normal gravity environment (gravity vector pointing downwards). For this base case, the inlet velocity is 5 cm/s, the oxygen level is 25%, the sample width is 5 cm and the pyrolysis front ($X = 0$) is located in the middle of the column. Figure 3(A) shows the complete column with specimen located in the middle of the column. The flame is represented by the fuel vapor reaction (depletion) rate iso-surface corresponding to the value of 10^{-4} g/cm^3/s. The burnt fuel is shown shaded in light gray and the fresh fuel up-stream is shaded in dark gray. The fuel specimen is bounded by metal strip on

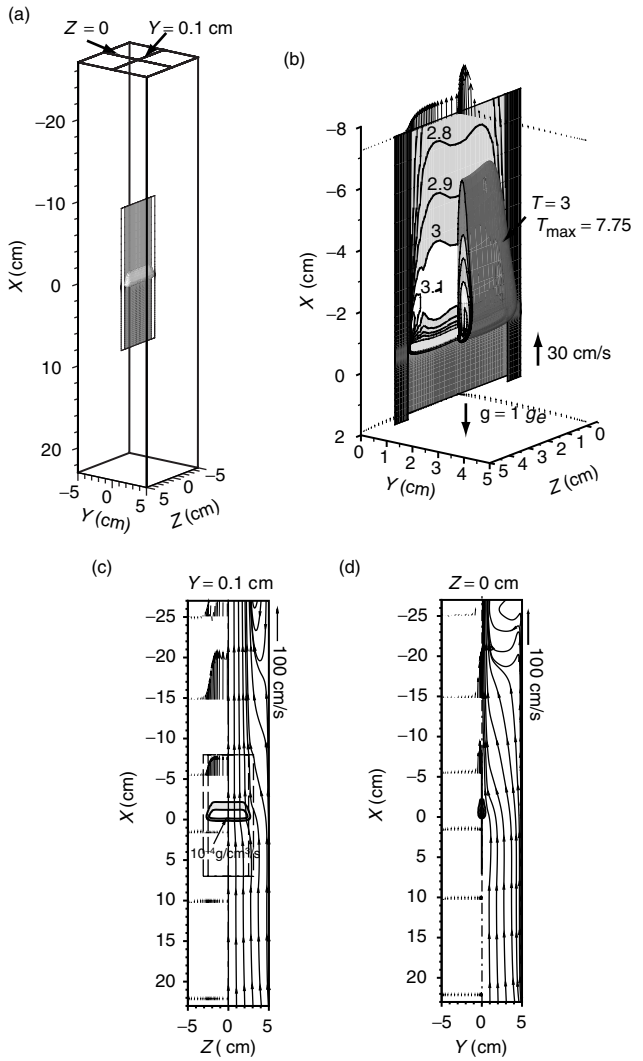

Figure 3: Simulation of fuel specimen burning inside the column under normal gravity environment (gravity vector pointing downwards). U_∞ = 5 cm/s and O_2 = 25%. Figure 3(A) shows the complete column with specimen located in the middle of the column. The flame is represented by the reaction rate iso-surface corresponding to the value of 10^{-4} g/cm^3/s. The burnt fuel is shown shaded in light gray and the fresh fuel up-stream is shaded in dark gray. The fuel specimen is bounded by metal strip on side. Figure 3(B) shows the close-up of flame zone represented by gas phase temperature contours/iso-surface and solid surface temperature distribution. Figure 3(C) and Fig. 3(D) show stream lines and velocity vector projections on planes at Y = 0.1 cm and Z = 0 cm respectively.

both sides. Figure 3(B) shows the close-up details of the flame region. Here the flame is represented iso-temperature surfaces. The outermost surface corresponds to temperature, $T = 3$ (where 1 unit = 300 K) followed by 3.5, 4, 5, 6 and 7. We note that the flame is essentially two-dimensional at the leading edge (except in regions close to the cold strips) and become three-dimensional downstream. Consequently the solid surface temperature distribution follows the gas phase temperature distribution. The surface temperature contours are horizontal near the flame leading edge and become two dimensional downstream. The three dimensional feature of the flame in the downstream region is consequence of the flow dynamics in the region. The hot combustion gases accelerate on account of buoyancy, there by entraining oxidizer from the sides and thus cooling the hot rising plume. Figure 3(B) also shows velocity vector distributions at two locations: one upstream of the flame and another downstream of the flame. The velocity vectors are plotted on the $Z = 0$ plane and on the $Y = 0.1$ cm plane. The velocity vectors upstream of the flame are small in magnitude representing small inlet velocity whereas at the downstream location in the flame region velocity vectors show increased velocity in the buoyant plume which decay away from the flame. The flow structure inside the entire column is more clearly depicted in figs. 3(C) and 3(D). Figure 3(C) shows streamlines and velocity vector projections on a plane parallel and above the fuel surface at $Y = 0.1$ cm. The projections of velocity vectors are shown on the left half and the curves on right half are constructed as two-dimensional streamlines using planar velocity components only to show the flow pattern in the plane. The flame is represented by the reaction rate contour of 10^{-4} g/cm^3/s. $X = 0$ is the location of the pyrolysis front (defined as the point of 5% solid burnout) along the centerline. This figure clearly shows combustion product accelerating due to buoyancy downstream of flame. Near the column exit the velocity at the center of the column exceeds 100 cm/s. A check on the magnitude of Rayleigh number shows that the flow continues to be laminar at the column exit. The downstream streamlines are seen converging towards the center where the accelerating product in the plume entrains the surrounding air. As all the mass of gas mixture fed at the bottom of the column is drawn towards the centrally rising plume, the ambient air (assumed free of contamination by combustion products) enters into column from the top opening through the regions near the column walls. Figure 3(D) shows similar flow details in $Z = 0$ symmetry plane. The difference in flow structure between fig. 3(C) and fig. 3(D) illustrates the 3D flow in the downstream region of the column.

4.2. Factors influencing ambient air entrainment

The phenomena of entrainment of ambient air into the column was explained in the above section based on the proposition that the accelerated hot combustion product plume entrains the surrounding column gases and when all the gas mass supplied to the column from the base of the column is drawn to the central plume, the column space is occupied by the ambient air entering from the top of the column. In this section, the effects of inlet flow velocity, sample size, sample location and column cross-sectional area on flow field and ambient air entrainment are investigated. In figs. 4 (A-F), the flow

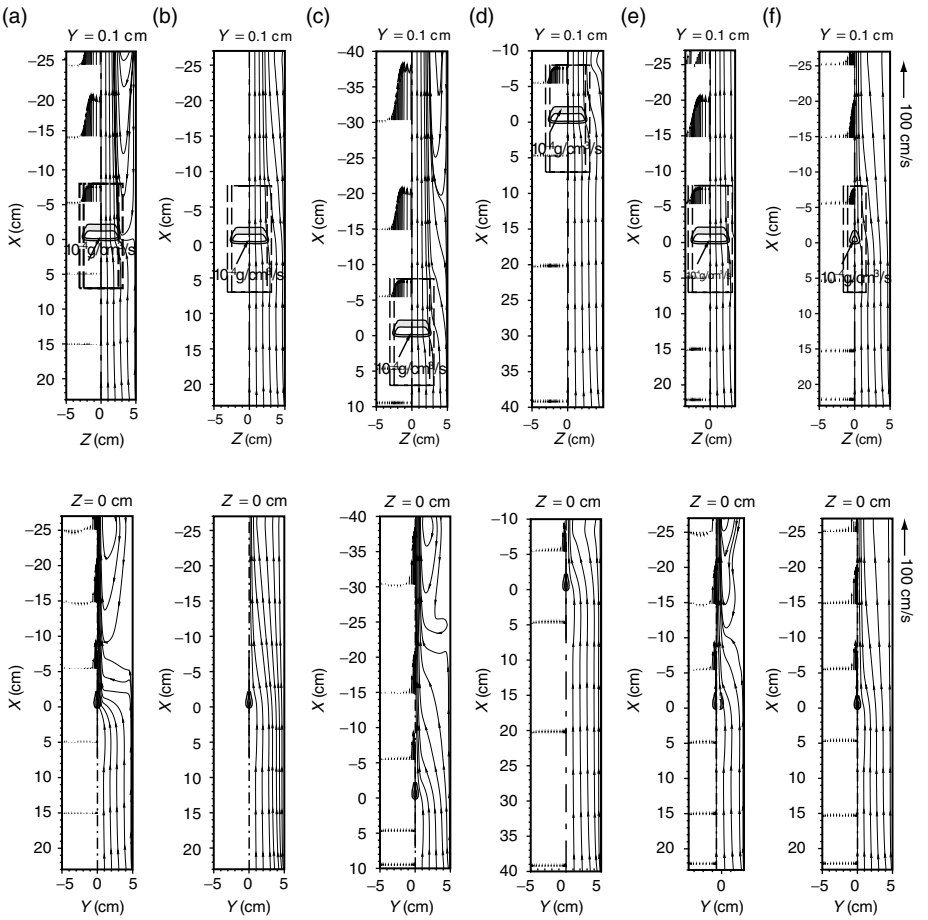

Figure 4: Effect of various parameters on ambient air entrainment into the column at 25% O_2 (compare with the base case shown in fig. 3C & fig. 3D. The figures A-F show projected velocity vectors and corresponding streamlines on planes $Y = 0.1$ cm above the fuel surface (upper) and at $Z = 0$ (lower). (A) $U_\infty = 0.5$ cm/s, (B) $U_\infty = 10$ cm/s, (C) flame position ($X = 0$), 40 cm below the column exit, (D) flame position at 10 cm below column exit, (E) tunnel cross section 7 cm × 7 cm and (F) fuel specimen 0.5 cm wide.

pattern in the column at $Y = 0.1$ cm plane (upper set of figure) and at $Z = 0$ (lower set of figures) are shown for different cases. Similar to fig. 3 (C) and (D), the left side of the figures shows projected velocity vectors and the right side shows the streamlines based on projected velocity field. The figures also show the position of the fuel sample and the flame is represented by the reaction rate contour of value 10^{-4} g/cm^3/s. In figures 4 (A) and (B) the column base inlet velocity is changed from the base case of

5 cm/s to 0.5 cm/s and 10 cm/s respectively. Change in inlet velocity changes the mass flow rate of gas mixture entering the column from the bottom. Figure 4 (A) shows that for a low inlet velocity, large amount of the ambient air is entrained into the column from the top opening. The entrained ambient air can reach close to the flame region. The stream lines (both at $Y = 0.1$ cm and $Z = 0$) are seen to sharply converge towards the central plume of hot gases indicating a complete entrainment of the gas mixture fed at the bottom happens over a very short distance downstream of the flame. On the other hand at a high inlet flow velocity as shown in fig. 4 (B) there is no entrainment of the ambient air into the column. The stream lines only show slight bend towards the central plume. In figures 4 (C) and (D) the positions of the fuel specimen inside the column are varied while the inlet flow velocity is fixed at 5 cm/s. Comparing these with figs. 3(C) and (D), it can be seen that a sample located deep inside the column (in fig. 4 (C), $X = 0$ is 40 cm below the column exit plane), produces a thermal plume from the combustion products that has higher velocities at the column exit. This is because the hot combustion products have more distance to accelerate from buoyant force. This larger plume mass flow rate results in a corresponding larger air entrainment from the top of the column. The entrained air reaches deeper into the column. However, the distance between the flame base and the entrained air lower location are approximately the same as in the base case (figs. 3 (C)). When the fuel sample is placed close to the column exit plane (in fig. 4 (D), $X = 0$ is 10 cm below exit plane), there is no air entrainment into the top opening since the thermal plume velocity there is still sufficiently low.

From the results of figures 4 (A-D), it appears that the amount of air entrainment into the column top opening is the result of mass imbalance between the inlet total mass feeding rate and the thermal plume outflow rate. In steady operation, total mass outflow rate is equal to total mass inflow rate. If the thermal plume produces an upward flow that exceeds the total mass feeding rate from the column bottom then ambient air entrainment into the column is inevitable. To test this explanation further, a couple of test cases are shown in figs. 4(E) and (F). In figure 4(E) the column section is reduced to 7 cm × 7 cm while the feeding velocity is fixed at 5 cm/s. Reduction of cross-sectional area reduces inlet total mass feed rate thus increased penetration depth of outside air into the column. It should be noted that in this case as the fuel specimen width (inclusive of strips) is 6.2 cm leaves a very small gap with the wall, therefore, the entrainment is seen here only in the Z plane. Finally fig. 4(F) presents a case of narrow fuel specimen (0.5 cm wide). Here the mass of combustion product is small and therefore although the plume velocity is same as in the base case presented in fig. 3, the small cross section of the hot plume cannot entrain all the column gasses. Hence no entrainment is observed.

Here it should be pointed out that Wharton in his work [4, 5] reasoned ambient air entrainment into the column solely based on local oxygen concentration measurements. The lack of detailedinformation on flow field led him to conclude that density difference between the mixture supplied into the column and the ambient air caused entrainment of air into the column. Wharton therefore, argued that for the materials with LOI less than that of ambient air, the lighter gas mixture could be displaced by denser ambient air from the column exit whereas testing materials with LOI greater than ambient air

would not be effected by the ambient air. It should also be noted that the density difference between the ambient air and the inlet gas mixture (for LOI value less than ambient) is always less than 4% so it is unlikely to effect the column composition reported in the experiment.

Figure 5 (A-E) presents quantitative comparison of entrainment. The plots show entrainment, represented as ratio of gas mass flow rate leaving the column at the top to the inlet gas mass flow rate at the bottom of the column, *i.e.* $\dot{m}_{out}/\dot{m}_{in}$, with the parameters affecting entrainment discussed in the section above (fig. 4). The computations for this parametric study were carried about the base case described earlier. When there is no ambient air entrainment, $\dot{m}_{out}/\dot{m}_{in} = 1$. The larger the value of $\dot{m}_{out}/\dot{m}_{in}$, the more is the ambient air entrainment relative to inlet gas mass feed rate. Figure 5 (A) shows effect of column base inlet velocity, U_{∞}, on entrainment. For cases with circular symbols, the inlet gas stream is at oxygen level of 25%. As column inlet velocity is decreased, $\dot{m}_{out}/\dot{m}_{in}$ increases (not shown here: the absolute value of $\dot{m}_{out}$ also increases). The approximate dependence of entrainment on inlet velocity is seen to follow $\dot{m}_{out}/\dot{m}_{in} \sim 1/\bar{U}_{\infty}^{0.85}$. It was noted that for cases with inlet flow velocity of 3 cm/s and 5 cm/s the entrainment-affected region did not reach the flame ($X = 0$) over the range of oxygen level from 25% down to extinction point. Only in case of inlet velocity of 0.5 cm/s the entrained air reached close to the flame stabilization zone. Figure 5(A) also shows points (gradient symbol) for flame near the extinction limit (O_2~19.6%) at base inlet velocity of 3 cm/s and 5 cm/s. These near flame extinction points remain close to the corresponding values for 25% oxygen cases, showing little effect of change in oxygen level on entrainment up to the point of extinction. Figure 5 (B) shows variation of entrainment with cross sectional area of the column ($\bar{A}_{CS} = \bar{H}_T \times \bar{W}_T$). The ASTM standard permits column diameter greater than or equal to 7.5 cm for the test. Three other columns with cross sectional areas 9 cm × 9 cm, 8 cm × 8 cm and 7 cm × 7 cm, which are all greater than cross sectional area for the standard column of 7.5 cm diameter ($\bar{A}_{CS}$ = 44.18 cm^2), are used to study the effect of column dimension on entrainment. The entrained air increases as the column cross section is reduced, so a column with smaller cross section for a given fuel sample type and size is more prone to entrainment compared to a column with larger cross section. However, in the present computation, for all the four columns the gas composition near the flame stabilization region was unaffected by the entrainment and the computed flame spread rates were identical (V_f = 0.57 cm/s) for all the four column cross-sectional dimensions.

The computed result show $\dot{m}_{out}/\dot{m}_{in} \sim 1/\bar{A}_{CS}^{0.8} = 1/H_T^{1.6}$ (as $\bar{H}_T = \bar{W}_T$ in all cases). Figure 5 (C) shows the effect of fuel sample position in the column on ambient air entrainment. As the sample is lowered in the column, the rising plume causes an increase in ambient air entrainment into the column. The computation show $\dot{m}_{out}/\dot{m}_{in} \sim 0.526 + 0.054\ \bar{x}_{exit}^{0.8}$ where $\bar{x}_{exit}$ is distance of flame stabilization point from the column exit plane. In fig. 5 (D) the effect of sample width, $\bar{W}_F$ on entrainment is shown. As the sample width is increased the entrainment in the column increases. The computation indicates a trend $\dot{m}_{out}/\dot{m}_{in} \sim 0.015 + 0.3908\ \bar{W}_F^{0.73}$. Figure 5 (E) illustrates the effect of gravity on the entrainment. As gravity is reduced (Earth, Martian and Lunar) entrainment effect is found to decrease with approximate dependence

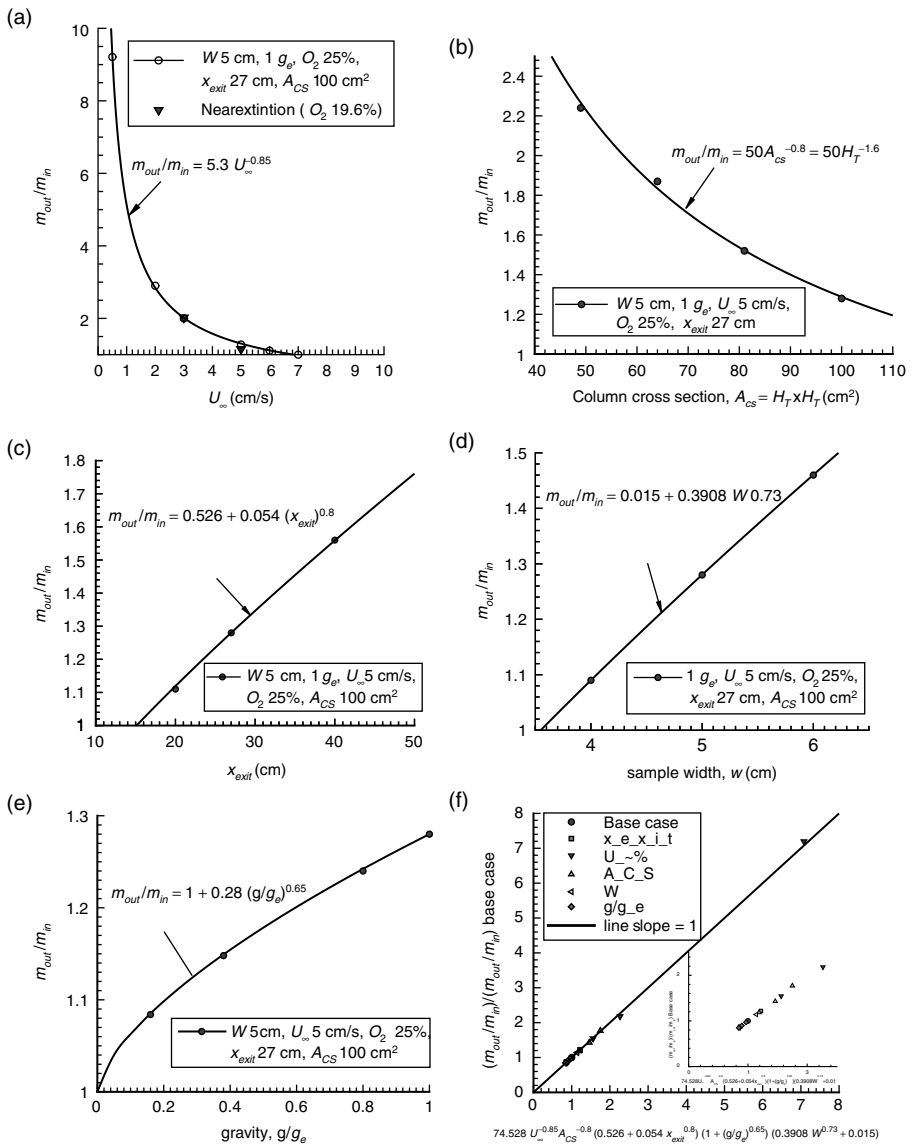

Figure 5: Parametric study on factors affecting air entrainment into the column. Entrainment is represented by the ratio $\dot{m}_{out}/\dot{m}_{in}$ (A) effect of U_{∞}, (B) effect of column cross sectional area, (C) effect of sample position, (D) effect of fuel sample width, (E) effect of gravity, (F) numerical correlation plot of computed data.

$\dot{m}_{out}/\dot{m}_{in} \sim 1 + 0.28\left(\bar{g}/\bar{g}_e\right)^{0.65}$. The computed parametric study can be summarized by the following numerical correlation for the ambient air entrainment:

$$\left(\dot{m}_{out}/\dot{m}_{in}\right)/\left(\dot{m}_{out}/\dot{m}_{in}\right)_{base\ case} = 74.528\,\bar{U}_{\infty}^{-0.85}\bar{A}_{CS}^{-0.8}\left(0.526 + 0.054\bar{x}_{exit}^{0.8}\right) \times\left(1 + 0.28\left(\bar{g}/\bar{g}_e\right)^{0.65}\right)\left(0.015 + 0.3908\bar{W}_F^{0.73}\right)$$

In the above correlation $\bar{U}_{\infty}$ is in cm/s, $\bar{A}_{CS}$ is in cm^2, $\bar{x}_{exit}$ in cm, $\bar{g}$ / $\bar{g}_e$ is non-dimensional acceleration due to gravity, normalized to gravitational acceleration at earth's surface and $\bar{W}_F$ is in cm. The base case corresponds to the parametric values O_2 = 25%, $\bar{U}_{\infty}$ = 5 cm/s, $\bar{A}_{CS}$ = 100 cm^2, $\bar{x}_{exit}$ = 27 cm, $\bar{g}$ / $\bar{g}_e$ = 1 and $\bar{W}_F$ = 5 cm/s. All the computed data are plotted in Fig. 5 (F) using this correlating parameter. Note that the ranges of each physical quantity in the correlation are limited as shown in fig 5 (A-E).

There are simplified theoretical analyses available in literature [11, 12], leading to similarity solution for entrainment in a vertically rising laminar plume from a heated point source and a horizontal line source in an infinite ambient. In the present study the fuel sample is of finite size (both width and height) placed inside a column with a flame (or heat release zone) also of finite size. To compare with these simplified analytic expressions, we note that the line source similarity solution gives $\dot{m}_{plume}/\dot{m}_{in} \sim g^{0.2}x^{0.6}/U_{\infty}H$ and the point source solution gives $\dot{m}_{plume}/\dot{m}_{in} \sim x/U_{\infty}H^2$. In comparison, we see some similarity of the trends on $\bar{U}_{\infty}$, $\bar{H}_T$ and $\bar{x}_{exit}$ but the gravity ($\bar{g}$ / $\bar{g}_e$) dependence show much larger difference. This correlation is based on limited computed points and needs validation by experiments.

4.3. Limiting oxygen index

Figure 6 shows the computed Limiting Oxygen Index (molar percentage) plotted against the inlet flow velocity and two gravity levels ($1g_e$ and $0g_e$). The curves corresponding to normal gravity ($1g_e$, solid line curves) are discussed in this section and for micro-gravity ($0g_e$, dashed curves) are discussed in the next section. The way computed LOI is obtained resembles that of the actual test procedure. First, a converged steady flame solution is obtained in a high oxygen mixture flow. The oxygen level is then reduced with the previously converged steady solution as the initial input until new converged solution is obtained. This procedure is repeated with successfully reduced levels of oxygen in the mixture to determine limiting oxygen level to the desired accuracy that will support combustion. It should be noted that some materials exhibit near-limit oscillation. This is not treated in this model.

The solid curve with circle symbols in fig. 6 shows the variation of LOI with imposed flow velocity over the range 0.5 cm/s to 15 cm/s for a 5 cm wide specimen in normal gravity. The LOI value for all practical purposes can be considered a constant value. However, there is a slight trend of increased LOI with velocity. This is consistent with the known trend in the case of opposed flow flame spread at high air velocities where the flow residence time reduce and approaches reaction rate time

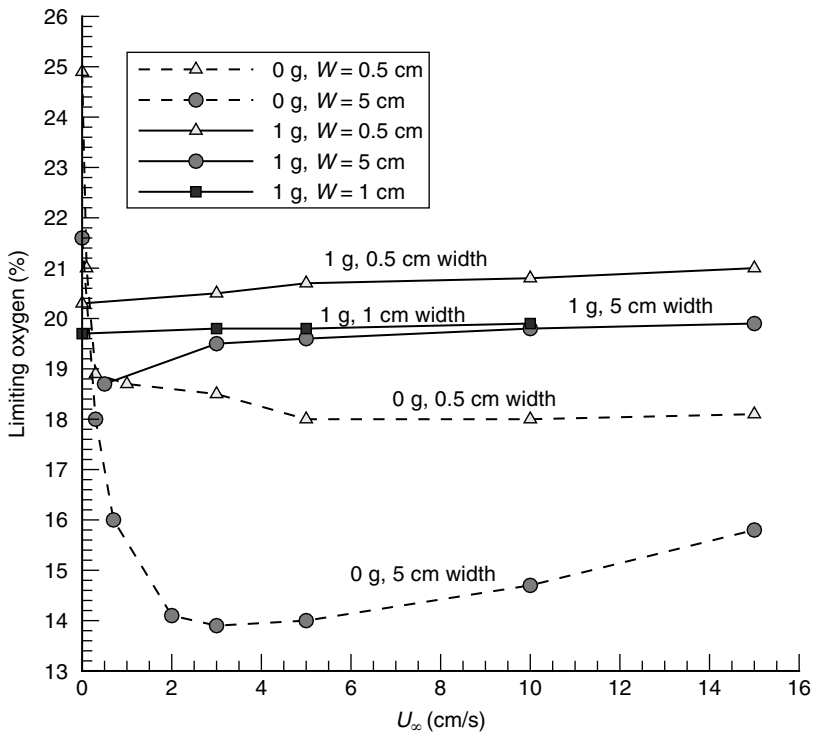

Figure 6: Computed Limiting Oxygen Index as a function of column inlet velocity. The solid curves correspond to LOI for specimens (5 cm, 1 cm and 0.5 cm wide) under normal earth environment. The dashed curves correspond to LOI for specimens (5 cm & 0.5 cm wide) in microgravity environment.

scales in the flame stabilization zone [13]. We can also see that at U_∞ of 0.5 cm/s the curve shows a steeper dip. This is caused by the influence of entrained air into the neighborhood of the flame leading edge as indicated in fig. 3(A). Since the ambient air has a higher oxygen percentage than that in the feed mixture, it causes additional oxygen supply into the flame through diffusion and lowers the LOI measured from the feed mixture. The plots also show LOI values computed for specimen with widths of 1 cm (solid curve with square symbols) and 0.5 cm (solid curve with triangle symbols). The LOI for 1 cm wide sample remains close to that of the 5 cm wide specimen except for $U_\infty < 3$ cm/s. As demonstrated before, a narrower sample causes less ambient air entrainment into the column. Therefore, the reason for the LOI dip in low U_∞ for the 5 cm case is absent for the 1 cm sample. On the other hand, the LOI values for 0.5 cm wide specimen are higher for all U_∞. This is due to the increasing three-dimensional heat loss from the narrow sample in the flame stabilization zone. Smaller flame has higher surface to volume ratio which enhances heat loss relative to the heat generation in the flame.

4.4. Computational results in microgravity

In addition to normal gravity results, selected computations are performed for zero-gravity conditions. The comparison between the normal-gravity and micro-gravity cases highlights the effect of gravity. In addition, the use of an open-ended flow channel is an option under consideration in space experiment in the International Space Station [14]. It is well known that both the solid spread rate and the extinction limit in opposed-flow in microgravity are sensitive to the air velocity when the velocities are small [13, 15, 16]. The open-ended tunnel is simple and cheap device that can be placed in a large chamber (e.g. glove box or CIR chamber) to effect a flow velocity change. Figure 7 shows a computed case with zero-gravity for conditions identical to one shown in fig. 3. The flame (fig. 7 (A)) is much longer and thicker compared to the normal gravity flame presented in fig. 3(B).The fuel surface temperature is also lower as the flame standoff distance from the fuel surface is larger in the open tipped microgravity flame compared to the closed tip flame in normal gravity.The absence of entrained flow at the open end is obvious (fig. 7(B) and 7(C)). The flow field is characterized by velocity magnitude one order lower than that seen in the normal gravity case. Further the stream lines are seen to diverge in the flame due to thermal expansion in contrast converging towards the fuel surface in presence of buoyant acceleration of the hot combustion products. Going back at the LOI, fig. 6 also shows two curves corresponding to microgravity environment

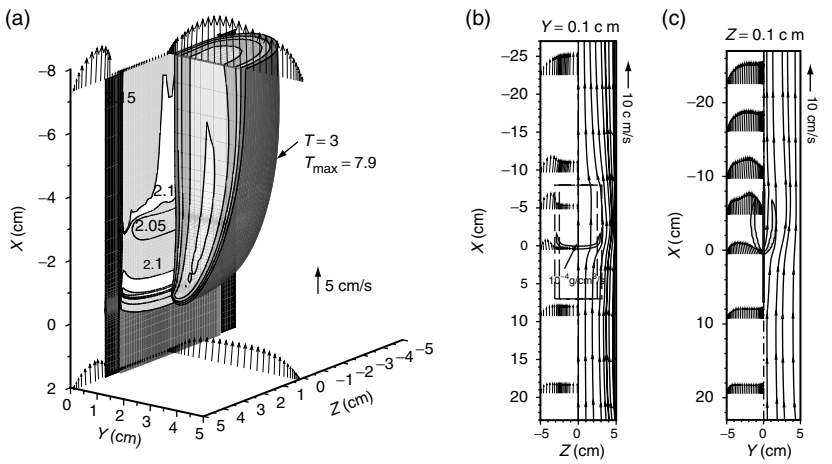

Figure 7: Simulation of burning of fuel specimen inside the column in zero-gravity environment. U_∞ = 5 cm/s and O_2 = 25%. Figure 7(A) shows the close-up of flame zone represented by gas phase temperature contours/iso-surface and solid surface temperature distribution. The burnt fuel is shown shaded in light gray and the fresh fuel up-stream is shaded in dark gray. The fuel specimen is bounded by metal strip on side. Figure 7(B) and Fig. 7(C) show stream lines and velocity vector projections on planes at Y = 0.1 cm and Z = 0 cm respectively.

(dashed curves). The LOI curve for the 5 cm wide specimen at zero-gravity (with circle symbols) is a non-monotonic curve with a minimum at about 3 cm/s. This non-monotonic trend manifests a Damkohler-number limited high-speed blow-off limit vs. a heat-loss limited low-speed quenching limit as first identified experimentally in [15]. The heat losses in this case can be from both surface radiation and gas radiation. In the present model only surface radiation loss is included. More detailed gas radiation contributions have been investigated by [17–19]. In solid combustion, surface radiative loss normally has more impact on flame extinction than gas radiation [19, 20]. Gas radiation has two opposing effects, namely gas radiation loss and heat feedback to the solid. The two effects are seen to balance each other approximately [19, 20]. So the presented computed LOI curves should give the correct qualitative trend and reasonable quantitative extinction limits. We observe that except in the very low velocity region, the LOI in zero gravity are lower than those in normal velocity that can have practical implication to spacecraft fire safety. An LOI curve for 0.5 cm wide fuel specimen is also shown in the figure. The LOI values are higher than for 5 cm wide specimen which is due to higher conductive/convective heat losses relative to heat generation for the narrower sample. Compared with the normal gravity case, there is larger LOI difference between the 0.5 cm wide and 5 cm wide cases. This is because in zero gravity the flame (or standoff) thickness is greater and the heat generation rate is smaller. A sample in zero gravity is non-dimensionally narrower than the same sample in normal gravity and the non-dimensional conductive/convective heat loss is amplified. Although many of the gravity effect on flames have been computed previously using one-or two-dimensional models. The study on the effect of finite fuel sample width requires use of a three-dimensional model such as this.

For completing the discussion on opposed flow type flame spread encountered in the LOI apparatus we finally look at the flame spread rates (V_f). Although the LOI apparatus is normally not used to study flame spread, thespread rateis an important parameter of practical interest for describing flame over a solid surface. Figure 8 shows the plots of variation in flame spread rate with opposing velocity magnitude at 25% oxygen for various fuel widths. The flame spread rates are plotted for both normal gravity (solid curve) and microgravity (dashed curves) conditions.The flame spread rates for the two gravities show different trends. In microgravity there exists a maximum V_f at some velocity whereas the normal gravity flame spread rate is nearly constant (decreasing very slightly with increase in inflow velocity). While the higher sensitivity of the microgravity flame and non-monotonic flame spread rate trend with velocity have been demonstrated and explained previously by both experiments [10, 15] and numerical simulations [9, 13], it is interesting to note that the maximum V_f occurs for narrow width fuel strips at higher inflow velocities. For example in case of 5 cm wide fuel strip maximum V_f occurs at inlet velocity of 5 cm/s but the maxima V_f's for 2 and 1 cm wide fuel strips occur at just 8.2 cm/s and about 15 cm/s respectively. For the 0.5 cm wide fuel strip the V_f is still increasing at inlet velocity of 15 cm/s. However, the maximum V_f for narrower sample is generally lower than that for broader samples due to higher heat loss from flame per unit heat generation in the flame volume. One can also note that the flame spread rate curves for $1g_e$ and $0g_e$ can cross-over especially for

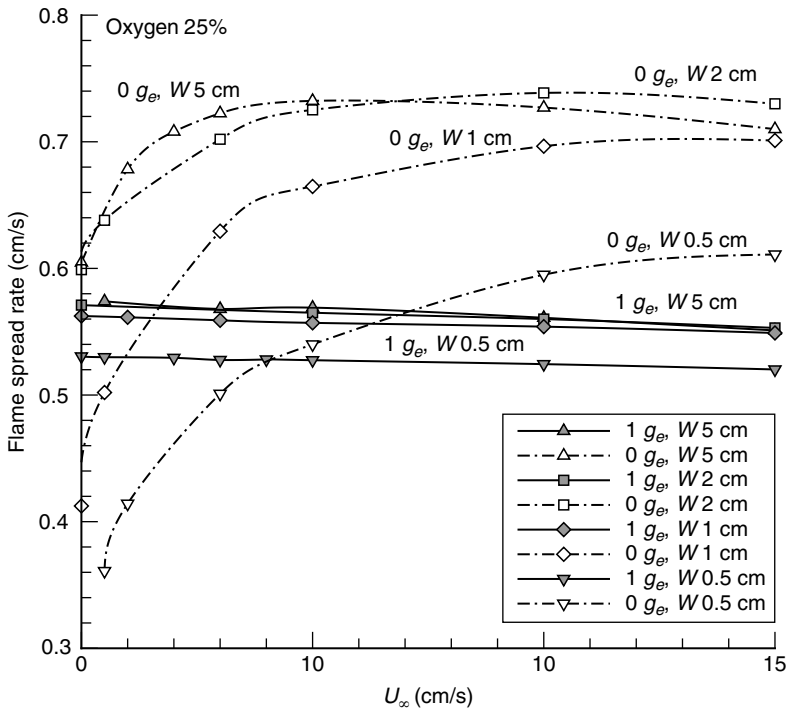

Figure 8: Variation of flame spread rate with inlet velocity at 25% O_2 in a tunnel of cross-section 10 cm × 10 cm for various fuel widths ranging from 0.5 cm to 5 cm. The solid curves are for 1g and the dashed curves are for 0g.

narrow width fuel strip and at low oxygen levels. The flame spread rates for $1g_e$ cases are seen to become independent of fuel width for fuel width greater than 1 cm where as for the $0g_e$ case this is about 2 cm.

5. CONCLUSION AND ADDITIONAL REMARKS

From this numerical study on straight column limiting oxygen index apparatus the following conclusions can be drawn:

1) Detailed three-dimensional flow patterns have been computed in the LOI apparatus. Ambient air can be entrained into the column. This is caused by buoyant acceleration of the combustion products. If, at the column opening, the mass outflow rate in the combustion/thermal plume exceeds the O_2/N_2 mixture flow feeding rate at the bottom of the column, ambient air will enter into the column from the top opening.
2) The amount of entrained air and its depth of penetration into the column depend on how much is the imbalance between the above two flow rates. This imbalance can be affected by the sample size, the sample location and the column cross-sectional

area in addition to the feeding velocity in normal earth gravity tests. A correlation based on the numerical data obtained from parametric study is given for estimating the non-dimensional ambient air entrainment into the test column.

3) In the suggested range of feeding velocities between 3 cm/s and 12 cm/s, the computed LOI for all practical purposes can be taken to be independent of the velocity in support of the claim by the designers of the test [2].
4) For specimen with width less than 1 cm, the computed results show a higher LOI. For these narrow samples, three-dimensional effect such as lateral heat loss renders the sample less flammable. LOI for sample width greater than 1 cm show little dependence on width. This is consistent with previous studies [21, 22] and the recommended test specification for thin materials.
5) In zero gravity there is no buoyant flow and no gravitational acceleration in the thermal plume. Therefore, there is no ambient air entrainment into the column from the top. Also, because of the lack of buoyant flow component, the LOI becomes more sensitive to the feeding velocity. The computed LOI boundary varies with the flow velocity in a non-monotonic manner similar to that found previously in microgravity experiment [15]. For the velocity range between 1 and 15 cm/s, the computed LOI in microgravity (purely forced flow) is lower than those in normal gravity (mixed forced and buoyant flow).
6) Compared to the normal gravity flame, the flame spreads rates are more sensitive to fuel width and opposing velocity magnitude in microgravity environment and the maxima in the flame spread rate in microgravity for the narrow fuel strip occurs at a higher opposing velocity magnitude compared with a broader fuel sample. The flame spread rates curves in microgravity and normal gravity exhibit a cross over. Microgravity flame spread rates were observed to be lesser than normal gravity flame spread rates typically at low oxygen levels and or low inflow velocities.

It should be pointed out that in the present study the fuel specimen is assumed to be thin so that the flame can only be stabilized on the two sides of the sample. In thick samples, the flame can also be stabilized in the wake region behind the top end of the specimen [23, 24]. In a previous numerical study [25] it was shown that whether the flame will stabilize on the side or on the top of a thick fuel depends on the flow and oxygen conditions. In addition to the existence of a bifurcation zone, the LOI trend for the two flames (side stabilized and wake stabilized) with flow velocity was different for a thick solid. While the LOI for side-stabilized flame gradually increases with flow velocity (over 0–40 cm/s), the LOI of wake-stabilized flame decreases with flow velocity. Also, it should be noted that the standard testing procedure requires fuel specimen to be placed in between metallic strips, however it was shown in [26] that in case the fuel is allowed to burn along the edges the LOI values can get affected drastically and even reverse the trend between $0g_e$ and $1g_e$ reported here.

ACKNOWLEDGEMENT

This research was supported by NASA grant NNC04AA58A.

REFERENCES

[1] Standard test method for measuring the minimum oxygen concentration to support candle-like combustion of plastics (Oxygen Index). Annual book of ASTM standards, 8(4) 278–282.

[2] Fenimore CP, Martin FJ, Candle-type test for flammability of polymers. Modern Plastics, 1966:43 141–148.

[3] DiPietro J, Stepniczka H, Factors affecting the Oxygen Index flammability ratings. SPE Journal, 1971:27 23–31.

[4] Wharton RK, Comments on the effect of gas velocity on Oxygen Index measurement. Journal of Fire Sciences, 1983:1 459–464

[5] Wharton RK, Anomalous behaviour in certain versions of the Critical Oxygen Index testing columns under ambient conditions. J. Fire and Materials, 1981:5(1) 6–13

[6] McIlhagger R, Hill BJ. The influence of sample dimensions on the Critical Oxygen Index of thin polypropylene films. J. Fire and Materials, 1981:5(3) 123–127.

[7] Zhevlakov AF, Kondrikov B, Bolodyan IA., Effect of gas flow velocity on the Oxygen Index of polymer materials. Combust. Explosion, Shock waves, 1983:19(5) 545–547

[8] Smooke MD, Giovangigli V. Formulation of the premixed and non-premixed test problem. Lecture Notes in Physics, Series 384, Springer-Verlag, New York, 1991, Chapter 1.

[9] Kumar A, A numerical model of opposed flow flame spread over thin solid fuels, 2004. PhD. Dissertation, Case Western Reserve University, Cleveland, OH.

[10] Olson. S. L., The effect of microgravity on flame spread over a thin fuel, NASA TM-100195(1987), Lewis Research Center, Cleveland, OH, 1987.

[11] Fuji T, Theory of the steady laminar natural convection above a horizontal line heat source and a point heat source. Int. J. Heat Mass Transfer, 1963: 6, 597–606

[12] Martynenko OG, Korovkin VN and Sokovishin YU A, The class of self-similar solutions fro laminar buoyant jets. Int. J. Heat Mass Transfer, 1989:32(12) 2297–2307.

[13] Kumar A, Shih HY, T'ien JS, A comparison of extinction limits and spreading rates in opposed and concurrent spreading flames over thin solids. Combust. Flame, 2003:132 667–677.

[14] Ferkul, P.F., Private communication, 2012.

[15] Olson SL, Ferkul P. V., T'ien JS, Near-limit flame spread over a thin solid fuel in microgravity. 22nd Symposium (International) on Combustion, The Combustion Institute, 1988, 1213–1222.

[16] Altenkirch, RA, and Bhattacharjee, S, Opposed-flow flame spread with implications to combustion in microgravity, *Prog. in Aero. and Astro.* AIAA, 1990. 723–740.

[17] Kumar A, Tolejko K, T'ien JS, A Computational study of flame-solid radiative interaction in flame spread over thin solid-fuel. J. Heat Transfer, 2004:126, 611–620.

[18] Rhatigan, J. L., Bedir, H., and T'ien, J. S., "Gas-Phase Radiative Effects on the Burning and Extinction of a Solid Fuel," Combust. Flame, 112:231–241 (1998).

[19] Kumar C. and Kumar A., On the role of radiation and dimensionality in predicting flow opposed flame spread over thin fuels. Combust. Theory and Modelling 16(3), 2012, 537–569.

[20] Bhattacharjee S. and Altenkirch R.A., Radiation controlled, opposed-flow flame spread in a microgravity environment, Proc. Combust. Inst. 23 (1990), 1627–1633.

[21] Frey Jr. A E, T'ien JS, Near-limit flame spread over samples. Combust. Flame, 1976:26 257–267.

[22] Sibulkin M, Kettlehut W, Feldman S, Effect of Orientation and external flow velocity on flame spreading over thermally thin paper strips. Combustion Science and Technology, 1974:9 75–77.

[23] Halli Y, T'ien JS, Effect of convective velocity on upward and downward burning limits of PMMA rods. National Bureau of Standards, NBS-GCR-86–507, 1986.

[24] Sibulkin M, Little M. W., Propagation and extinction of downward burning fires. Combustion and Flame, 1978:31 197–208.

[25] Kumar A, T'ien J. S., A Computational study of Low Oxygen Flammability limit for thick solid slabs. Combustion and Flame, 2006:164 366–378.

[26] Kumar C. and Kumar A., Computational Study on Opposed Flow Flame Spread Over Thin Solid Fuels with Side-Edge Burning. Combust. Sci. Tech.182(9), 2010, 1321–1340.